

# Electronic Phase Separation in the Hexagonal Perovskite $\text{Ba}_3\text{SrMo}_2\text{O}_9$

S. Simpson<sup>1</sup>, S. Fop<sup>1</sup>, H. A. Hopper<sup>1</sup>, G. B. G. Stenning<sup>2</sup>, C. Ritter<sup>3</sup>, and A. C. McLaughlin<sup>1\*</sup>

<sup>1</sup> *Chemistry Department, University of Aberdeen, Meston Walk, Aberdeen, AB24 3UE, U.K.*

<sup>2</sup> *ISIS Experimental Operations Division, Rutherford Appleton Laboratory, Harwell Science and Innovation Campus, Didcot, OX11 0QX, U.K.*

<sup>3</sup> *Institut Laue Langevin, 71 Avenue des Martyrs, BP 156, F-38042 Grenoble Cedex 9, France.*

Competition between exotic magnetic and electronic ground states underpins the properties of strongly correlated transition metal oxides and can result in electronic phase separation (EPS). The 6H-perovskite  $\text{Ba}_3\text{SrMo}_2\text{O}_9$  exhibits no magnetic order down to 1.6 K and EPS is observed at 230 K. The ground state of this material contains a complex mixture of spin-singlet  $\text{Mo}_2\text{O}_9$  dimers and quasi-molecular  $\text{Mo}_2\text{O}_9$  clusters. Segregation in  $\text{Ba}_3\text{SrMo}_2\text{O}_9$  emerges due to competition between direct Mo–Mo bonding and Mo–O–Mo magnetic superexchange, comprising a novel mechanism of electronic phase separation in transition metal oxides.

## INTRODUCTION

Electronic phase separation (EPS) is a striking phenomenon that is observed in strongly correlated transition metal oxides (TMOs) when two or more electronically distinct phases emerge and coexist on a microscopic scale [1]. Remarkable physical properties, such as colossal magnetoresistance (CMR) in manganite perovskites, are typically associated with EPS [2–5]. Segregation can be induced in TMOs via chemical doping or changes in physical parameters such as temperature or magnetic field. Complex interplay between spin, orbital, lattice, and charge degrees of freedom typifies electronically phase-separated systems [6,7], leading to a number of closely competing ground states. For example, in the case of CMR manganites, chemical doping on the Mn site results in competition between a double-exchange ferromagnetic metallic phase and a charge/orbital-ordered antiferromagnetic (AFM) phase [8,9]. EPS is well documented in TMOs containing  $3d$  transition metals; however, it is rarely encountered in  $4d/5d$  TMOs.

Particular attention has recently been devoted to  $4d/5d$  TMOs exhibiting the six-layer hexagonal (6H)  $Ba_3B'M_2O_9$  ( $B'$  = lanthanide;  $M$  = Ru, Ir) structure type. Here, corner-sharing  $B'O_6$  octahedra connect layers of face-sharing bioctahedral  $M_2O_9$  dimers as shown in Fig. 1(a). These structural motifs form geometrically frustrated triangular sublattices within the  $ab$  plane, presenting ideal conditions in which to realize exotic ground states such as the quantum spin liquid [10–14]. Each individual  $MO_6$  octahedron is trigonally distorted due to interactions between  $M$  ions in neighboring octahedra [Fig. 1(b)]. Short  $M$ – $M$  separations, combined with spatially diffuse  $4d/5d$  orbitals, can then enable hybridization of the metal orbitals [15,16] [Fig. 1(c)]. Despite the potential for  $M$ – $M$  orbital hybridization in this structure type, the vast majority of  $Ba_3B'M_2O_9$  compositions feature magnetic moments localized on the  $M$  cations [17–21] so that Hund's coupling precludes  $M$ – $M$  bond formation [22,23]. However, close competition between the  $M$ – $M$

interactions and Hund's coupling can allow for magnetic spins on the  $M$  atoms to couple and dimerize, resulting in quasi-molecular  $M_2O_9$  clusters [24–26]. These clusters are characterized by gapped spin excitations as seen in  $Ba_3B'Ru_2O_9$  ( $B' = Na, Ca$ ) [24,27], where an energy gap opens between nonmagnetic singlet ( $S = 0$ ) and excited triplet ( $S = 1$ ) states.

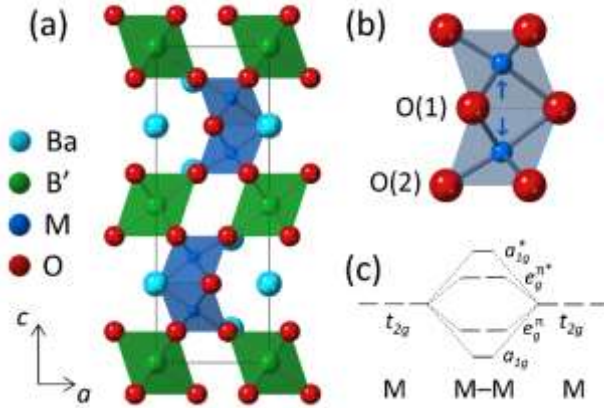


**Fig. 1.** (a) The crystal structure of  $Ba_3B'M_2O_9$  depicted in the conventional  $P6_3/mmc$  space group and projected down  $[100]$ . (b) Close-up view of the  $M_2O_9$  dimers: the octahedra are trigonally distorted, displacing each  $M$  cation away from the center of their respective octahedron (as indicated by the arrows) and resulting in two crystallographically inequivalent oxygen sites. (c) Partial energy level diagram for strongly interacting  $M_2O_9$  dimers, highlighting the consequent splitting of hybridized  $t_{2g}$  orbitals in a trigonally distorted environment.

Here, we report electronic and magnetic phase separation in the novel 6H-perovskite  $Ba_3SrMo_2O_9$ . Although  $A_3MnMo_2O_9$  ( $A = Sr, Ba$ ) compositions have been previously reported [28], these crystallize as disordered double perovskites. This is therefore the first 6H- $Ba_3B'M_2O_9$  composition where  $M = Mo$ , representing a new class of  $Ba_3B'M_2O_9$  materials.  $Ba_3SrMo_2O_9$  segregates into two structurally distinct phases at 230 K with both phases containing  $Mo_2O_9$  spin

dimers. We propose this segregation has an unusual electronic origin arising from competition between direct Mo–Mo bonding and antiferromagnetic Mo–O–Mo superexchange.

Polycrystalline samples of Ba<sub>3</sub>SrMo<sub>2</sub>O<sub>9</sub> were prepared and characterized as described in the Supplementary Information (SI) [29].

## RESULTS AND DISCUSSION

Rietveld refinement from neutron powder diffraction (NPD) data confirms Ba<sub>3</sub>SrMo<sub>2</sub>O<sub>9</sub> crystallizes in the hexagonal  $P6_3/m$  space group at room temperature (RT). The Rietveld fit to the  $P6_3/m$  structural model is shown in Fig. S1 and selected crystallographic data are presented in Tables S1 and S2. The  $P6_3/m$  structure [Fig. 2(a)] accounts for additional octahedral tilting distortions about the [001] direction [Fig. 2(b)]. This differs from the conventional structure expected for 6H-perovskites, which instead tend to crystallize in the  $P6_3/mmc$  space group [Fig. 2(c)]. The oxygen occupancies refined to within  $\pm 1\%$  of their nominal values and so were fixed at 1 for the remainder of the refinements. Bond valence sum (BVS) calculations yielded a value of  $BVS(\text{Mo}) = 5.15(1)$ , which is in good agreement with the nominal +5 oxidation state. Rietveld refinement of both laboratory X-ray diffraction (XRD) and NPD data find no evidence of cation disorder between the Sr and Mo sites. Furthermore, the large differences in ionic radii for octahedral Sr<sup>2+</sup> (1.18 Å) and Mo<sup>5+</sup> (0.71 Å) [37] make cation disorder highly unlikely.

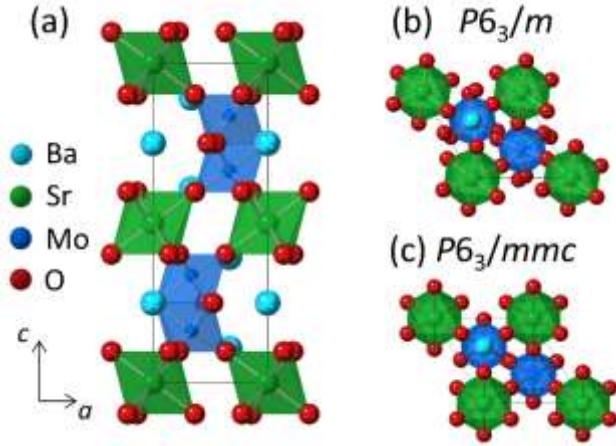


**Fig. 2.** (a) The 290 K crystal structure of  $\text{Ba}_3\text{SrMo}_2\text{O}_9$ , crystallizing in the  $P6_3/m$  space group as viewed down the  $[100]$  direction. (b) View of the  $P6_3/m$  structure down the  $[001]$  direction to highlight the presence of octahedral tilting distortions. (c) Equivalent  $[001]$  view of the parent  $P6_3/mmc$  structure, showing the lack of any analogous distortions compared to the  $P6_3/m$  structure.

$P6_3/m$  symmetry is retained down to 240 K, but below this temperature a new monoclinic  $P2_1/m$  phase emerges [Fig. 3(a)] accounting for two symmetrically inequivalent Sr and Mo sites. Close examination of the diffraction patterns also reveals a clear splitting of the  $(006)$  reflection below 230 K [Fig. 3(b)]. Rietveld refinement using a single  $P2_1/m$  phase could not account for this splitting. We tested all possible subgroups of both the  $P2_1/m$  space group as well as the  $P6_3/m$  parent space group, but none could reproduce the observed peak splitting. We also note that the multiplicity of the  $(00l)$  reflections is 2 and that peak splitting owing to a reduction in symmetry is not possible for these reflections. The anisotropic peak broadening method described by Stephens [38] has been successful in modelling anomalous peak broadening in  $6\text{H-Ba}_3\text{CaRu}_2\text{O}_9$  [27], but this did not improve the fit here. Instead, an excellent fit was obtained with a two-phase model consisting of  $P6_3/m$  and  $P2_1/m$  space groups (Fig. 4, Tables 1 and 2) so that phase separation is observed in  $\text{Ba}_3\text{SrMo}_2\text{O}_9$  for temperatures  $\leq 230$  K ( $T_{\text{PS}}$ ). The temperature dependence of the

weight fractions obtained from NPD Rietveld refinement is shown in Fig. 3(c). The two phases coexist over a large temperature range. High-resolution XRD and NPD measurements recorded at RT provide no evidence to suggest multiple phases are present above the structural phase transition so that phase separation is only observed at  $T_{PS}$ . Upon heating above  $T_{PS}$ , the  $P6_3/m$  phase is re-established as the primary phase. The phase composition appears to be highly sensitive to changes in the crystal structure. Phase segregation is observed at 230 K and the fraction of the  $P2_1/m$  phase grows upon cooling to a maximum of  $\sim 47.6(7)\%$  at 200 K. Below 200 K, there is a lattice anomaly for the  $P6_3/m$  phase [Fig. 5(a)] and with further cooling, the  $P2_1/m$  fraction decreases to  $\sim 42.2(7)\%$  at 150 K so that the  $P6_3/m$  phase becomes favorable. Below this temperature, there are no more significant changes in the crystal structure and the phase composition remains largely temperature independent. The data are modelled well with just two phases ( $P6_3/m + P2_1/m$ ) at all temperatures below 240 K so that the lattice anomaly for the  $P6_3/m$  phase does not arise from a further structural phase transition. There is also a strong lattice contraction along  $c$  for the  $P2_1/m$  phase at the structural phase transition [Fig. 5(b)].

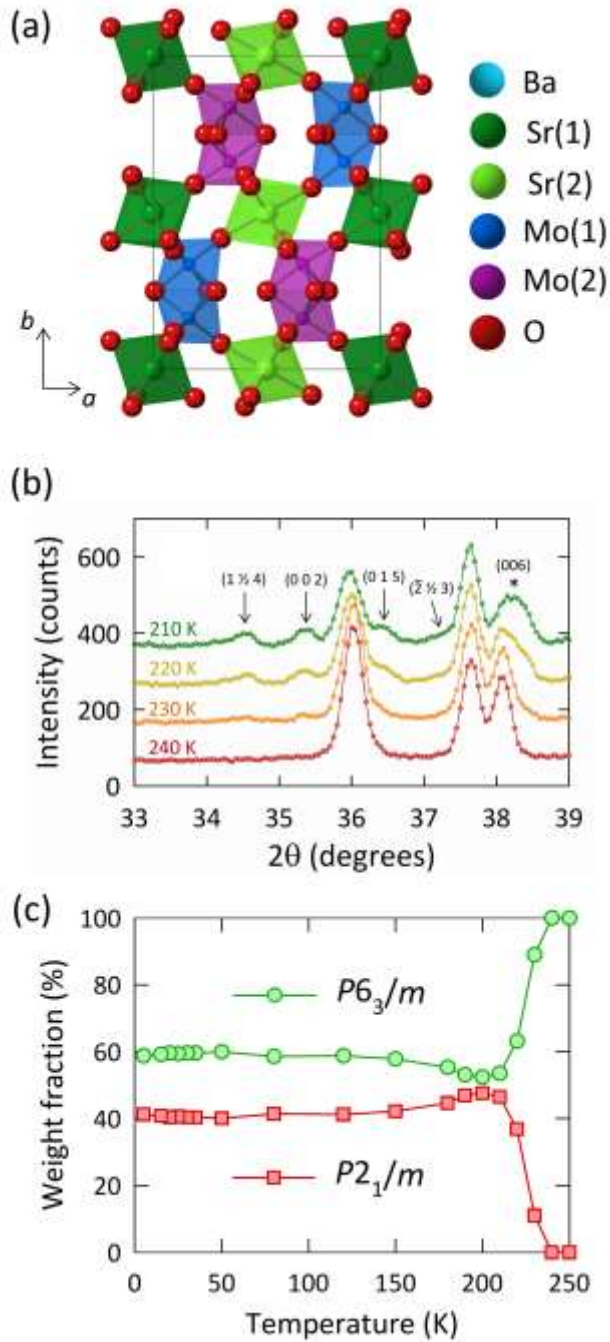


**Fig. 3.** (a) The  $P2_1/m$  structure of  $Ba_3SrMo_2O_9$  as viewed down the monoclinic  $[001]$  direction highlighting the crystallographically inequivalent  $Mo_2O_9$  dimers. (b) Evolution of the NPD patterns with temperature. Arrows denote the appearance of new reflections at 230 K consistent with the formation of a new  $P2_1/m$  phase, while the asterisk (\*) marks the splitting of the  $(006)$  peak as discussed in the main text. (c) Temperature dependence of the weight fractions at  $T \leq 230$  K; error bars are smaller than the data points.

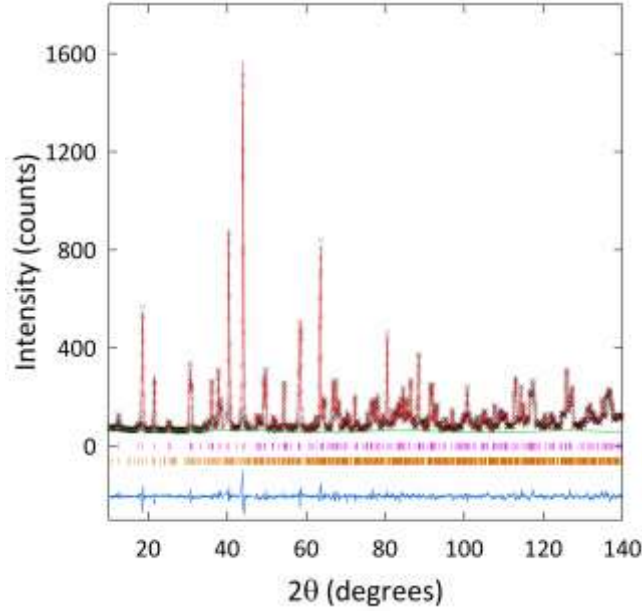


**Fig. 4.** The Rietveld fit to the two-phase  $P6_3/m$  (upper reflections) and  $P2_1/m$  (lower reflections) model from D2B NPD data collected at 5 K.

**Table 1.** Refined atomic parameters obtained from Rietveld fits to the two-phase  $P6_3/m$  and  $P2_1/m$  model using NPD data collected at 5 K. Refined cell parameters for each phase are provided in their respective table headings. Atomic displacement parameters have been constrained together according to the superscripts provided. The displacement parameters and the refined phase fractions were highly correlated, resulting in small  $U_{\text{iso}}$  values for the minority  $P2_1/m$  phase. The two phases were first refined separately in order to have the best starting point for the refinements; following this, they were refined together.  $R_{\text{wp}} = 5.80\%$ ,  $R_p = 4.39\%$ ,  $\chi^2 = 4.11$ .

$P6_3/m$  (5 K);  $a = 6.0507(1)$  Å,  $c = 14.6210(4)$  Å

Atom	Site	$x$	$y$	$z$	$U_{\text{iso}}$ (Å <sup>2</sup> )
Ba(1)	$2a$	0	0	1/4	0.013(2)
Ba(2)	$4f$	1/3	2/3	0.1078(4)	0.008(1)
Sr	$2b$	0	0	0	0.008(1)
Mo	$4f$	1/3	2/3	0.8375(3)	0.006(1)
O(1)	$6h$	0.5417(9)	0.0231(10)	1/4	0.019(1)
O(2)	$12i$	0.7771(6)	0.6370(7)	0.0974(2)	0.023(1)

$P2_1/m$ (5 K); $a = 12.1354(9)$ Å, $b = 14.5108(4)$ Å, $c = 6.0586(3)$ Å, $\beta = 119.93(1)^\circ$					
Atom	Site	$x$	$y$	$z$	$U_{\text{iso}}$ (Å <sup>2</sup> )
Ba(1_1)	2e	0.027(3)	3/4	-0.008(6)	0.000(1) <sup>1</sup>
Ba(1_2)	2e	0.509(3)	3/4	0.044(6)	0.000(1) <sup>1</sup>
Ba(2_1)	4f	0.165(2)	0.891(2)	0.674(5)	0.000(1) <sup>1</sup>
Ba(2_2)	4f	0.668(2)	0.895(2)	0.680(5)	0.000(1) <sup>1</sup>
Sr(1)	2a	0	0	0	0.003(2) <sup>2</sup>
Sr(2)	2b	1/2	0	0	0.003(2) <sup>2</sup>
Mo(1)	4f	0.163(2)	0.162(1)	0.664(4)	0.005(1) <sup>3</sup>
Mo(2)	4f	0.659(2)	0.165(1)	0.650(4)	0.005(1) <sup>3</sup>
O(1_1)	2e	0.283(2)	3/4	0.031(5)	0.001(1) <sup>4</sup>
O(1_2)	2e	-0.006(3)	3/4	0.518(6)	0.001(1) <sup>4</sup>
O(1_3)	2e	0.758(2)	3/4	0.483(5)	0.001(1) <sup>4</sup>
O(1_4)	2e	0.773(3)	3/4	0.007(5)	0.001(1) <sup>4</sup>
O(1_5)	2e	0.493(3)	3/4	0.475(6)	0.001(1) <sup>4</sup>
O(1_6)	2e	0.225(3)	3/4	0.400(4)	0.001(1) <sup>4</sup>
O(2_1)	4f	0.407(2)	0.882(2)	0.680(5)	0.001(1) <sup>4</sup>
O(2_2)	4f	0.701(2)	0.920(1)	0.236(3)	0.001(1) <sup>4</sup>
O(2_3)	4f	0.911(2)	0.881(2)	0.146(5)	0.001(1) <sup>4</sup>
O(2_4)	4f	0.929(2)	0.912(1)	0.638(3)	0.001(1) <sup>4</sup>
O(2_5)	4f	0.185(2)	0.909(1)	0.171(4)	0.001(1) <sup>4</sup>
O(2_6)	4f	0.428(2)	0.916(1)	0.257(3)	0.001(1) <sup>4</sup>

**Table 2.** Selected bond lengths (Å) for the  $P6_3/m$  and  $P2_1/m$  phases at 5 K.

$P6_3/m$ (5 K)			
Sr–O(2) x 6	2.390(3)	Mo–Mo x 2	2.557(8)
Mo–O(1) x 3	2.076(5)	Mo–O(2) x 3	1.871(4)
$P2_1/m$ (5 K)			
Sr(1)–O(2) x 2	2.43(3)	Sr(2)–O(2) x 2	2.41(3)
	2.30(2)		2.43(2)
	2.35(2)		2.45(2)
Mo(1)–O(1) x 2	2.10(3)	Mo(2)–O(1) x 2	2.10(3)
	2.05(3)		2.02(4)
	2.18(3)		2.00(3)
Mo(1)–O(2) x 2	1.86(3)	Mo(2)–O(2) x 2	1.87(3)
	1.88(3)		1.97(3)
	1.93(3)		1.85(3)
Mo(1)–Mo(1) x 2	2.56(4)	Mo(2)–Mo(2) x 2	2.46(4)

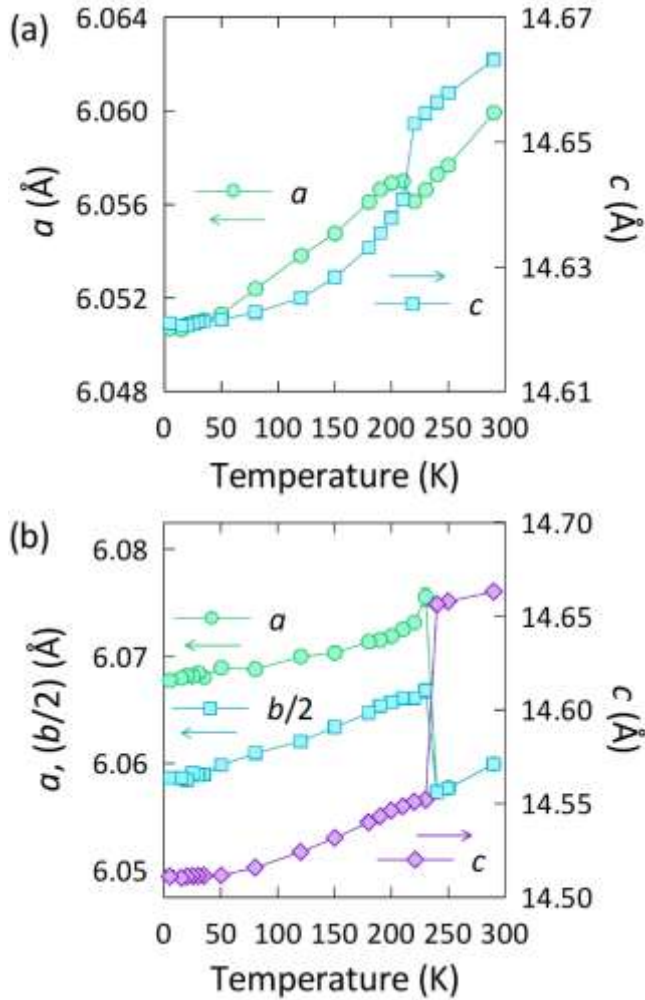


**Fig. 5.** Variation of lattice parameters with temperature for the (a)  $P6_3/m$  and (b)  $P2_1/m$  phases. Cell parameters for the  $P2_1/m$  phase have been normalized with respect to the parent  $P6_3/m$  structure for purposes of comparison. Where not apparent, error bars are smaller than the data points.

Variable temperature DC magnetic susceptibility measurements reveal there are two distinct changes in slope at  $T_1 \approx 240$  K and  $T_2 \approx 160$  K followed by a broad, asymmetric peak centered around 50 K (Fig. S2). The temperature variation of the susceptibility is reminiscent to that reported for  $Ba_3B'Ru_2O_9$  [25–27] and strongly suggests spin dimers are formed at low

temperatures. Heat capacity measurements [Fig. 6] reveal no magnetic ordering down to 2 K. Only a broad peak appears near 220 K, coinciding with  $T_{\text{PS}}$ . No anomaly appears near 160 K, showing  $T_2$  identified from magnetic susceptibility measurements does not arise due to any further structural or magnetic transition. There was also no evidence of magnetic diffraction peaks from high intensity neutron diffraction data on the D20 instrument down to 1.6 K. Our DC resistivity measurements found  $\text{Ba}_3\text{SrMo}_2\text{O}_9$  is too resistive to measure below 290 K, showing it is an insulator.

Phase separation is relatively uncommon in 6H-type  $\text{Ba}_3B'M_2\text{O}_9$  compositions. Segregation has been reported for  $\text{Ba}_3\text{CuSb}_2\text{O}_9$  where subtle variations in Cu/Sb stoichiometry can cause two phases to emerge at low temperatures [39]. This is induced by disorder over the  $B'$  and  $M$  sites in  $\text{Ba}_3\text{CuSb}_2\text{O}_9$ , but our XRD and NPD refinements ruled out this possibility in  $\text{Ba}_3\text{SrMo}_2\text{O}_9$ . Segregation has also been reported to occur in  $\text{Ba}_3\text{CoIr}_2\text{O}_9$  [40], though a fundamental understanding of its origins remains lacking. Symmetry-lowering distortions in  $\text{Ba}_3B'M_2\text{O}_9$  compositions are often related to the relative sizes of the  $B'$  and  $M$  cations [41–43], with larger  $B'$  cations causing greater distortions. For this reason, we also tested the possibility of partial disorder between the Ba and Sr sites in our Rietveld refinements; however, no evidence of significant disorder was found in either phase. Therefore, phase separation in  $\text{Ba}_3\text{SrMo}_2\text{O}_9$  does not appear to have a chemical origin.

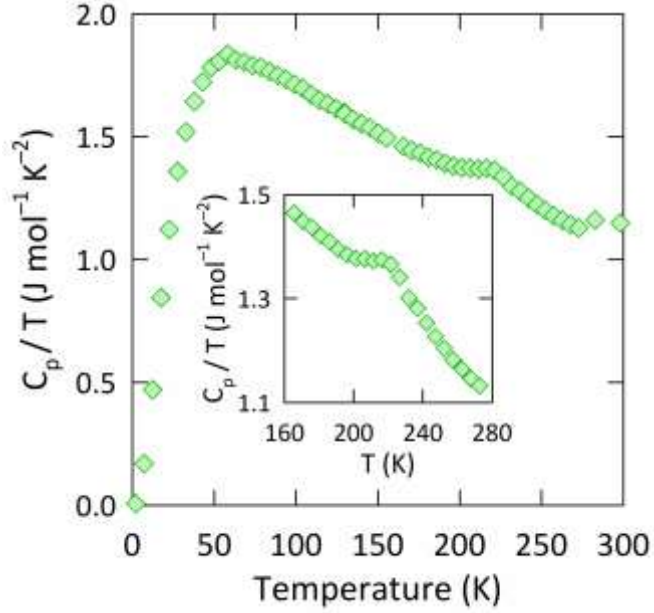


**Fig. 6.** Temperature dependence of the  $C_p/T$  ratio; the inset highlights the broad increase observed across the structural phase transition.

Another potential cause for the reduction in symmetry and phase separation is charge order as previously reported for  $\text{Ba}_3\text{NaRu}_2\text{O}_9$ , where the charge-ordered  $\text{Ru}^{5+}_2\text{O}_9$  and  $\text{Ru}^{6+}_2\text{O}_9$  dimers are characterized by a large difference in BVS values ( $\Delta\text{BVS} \approx 1$ ) [24,44]. However, our bond valence sum calculations (Fig. S3) show no significant anomaly at  $T_{\text{PS}}$ , so that charge order can be excluded as the mechanism for phase segregation in  $\text{Ba}_3\text{SrMo}_2\text{O}_9$ .

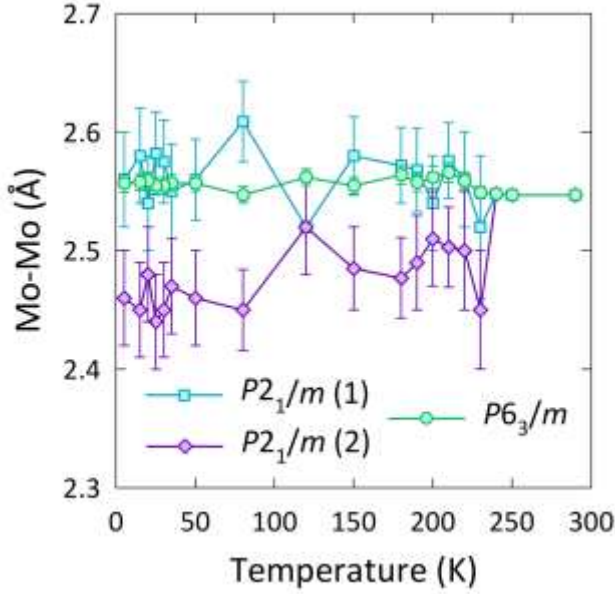


**Fig. 7.** Variation of Mo–Mo distances with temperature evidencing an orbital-ordering transition at  $T_{PS} = 230$  K.

Examination of the Mo–Mo distances [Fig. 7(a)] reveals the  $P6_3/m$  and  $P2_1/m$  phases are characterized by distinct Mo–Mo separations. Two unique  $P2_1/m$  Mo–Mo distances are observed owing to the two crystallographically inequivalent Mo sites in this phase. This suggests that it is the underlying Mo–Mo interactions which drive the observed segregation. Below  $T_{PS}$ , the  $P2_1/m$  Mo–Mo (2) distances are reduced by  $\sim 3.6\%$  compared to the Mo–Mo (1) distances and the Mo–Mo separation in the  $P6_3/m$  phase. Such a contraction in the  $M$ – $M$  distance is characteristic of an orbital-ordering transition accompanied by the formation of orbitally clustered molecular-like states [45]. The formation of orbital molecules in the  $P2_1/m$  phase is strongly coupled to the crystal lattice as shown by the strong lattice contraction along  $c$  below  $T_{PS}$  [Fig. 5(b)]. This is similar to electronically phase-separated  $\text{CaFe}_3\text{O}_5$ , in which trimeron formation is associated with a reduction in  $c$  below 300 K [46]. Hence, at  $T_{PS}$ , the Mo(2)  $t_{2g}$  orbitals have hybridized within dimers to form a direct Mo–Mo bond and quasi-molecular  $\text{Mo}_2\text{O}_9$  clusters. In contrast, the Mo–

Mo (1) distances are overall invariant with cooling; similarly, the  $P6_3/m$  Mo–Mo distances do not contract down to 5 K. This shows no Mo–Mo bond forms in the remaining Mo<sub>2</sub>O<sub>9</sub> dimers so that the Mo  $t_{2g}$  orbitals do not hybridize and their electrons remain localized.

Our susceptibility measurements indicated spin dimers form in Ba<sub>3</sub>SrMo<sub>2</sub>O<sub>9</sub>. These may be attributed to the localized Mo<sub>2</sub>O<sub>9</sub> dimers rather than the quasi-molecular Mo<sub>2</sub>O<sub>9</sub> clusters. It was not possible to fit the susceptibility data to a simple interacting dimer model [47] (Fig. S4). Instead, an excellent fit was obtained using a modified model with two interacting dimer terms as shown in Fig. 8. Each interacting dimer term accounts for the presence of a spin gap between the  $S = 0$  singlet and the  $S = 1$  triplet states, like Ba<sub>3</sub>B'*M*<sub>2</sub>O<sub>9</sub> ( $M = \text{Ru}$  and  $\text{Ir}$ ) compositions [24,27,34,48]. This model also includes a temperature-independent term to describe the susceptibility of the quasi-molecular Mo<sub>2</sub>O<sub>9</sub> clusters; this has previously been shown to be excellent at modelling the contribution to the susceptibility of the triplet excited state of orbital molecules mixing into the singlet ground state [49]. The full model is then given by the following expression:

$$\chi_{\text{total}} = A + \chi_p + 0.75\chi_{\text{dim}}(1) + 0.25\chi_{\text{dim}}(2) \quad (1)$$

where  $\chi_{\text{total}}$  is the total (molar) magnetic susceptibility,  $A$  is the temperature-independent term for the Mo<sub>2</sub>O<sub>9</sub> orbital molecules,  $\chi_p$  is a Curie-Weiss term accounting for paramagnetic impurity spins, and  $\chi_{\text{dim}}(1,2)$  refer to the susceptibility contributions from interacting spin dimers in the  $P6_3/m$  and  $P2_1/m$  phases, respectively. The Curie-Weiss term gave a Curie constant of  $C = 0.0168(5)$  emu K mol<sup>-1</sup> corresponding to a very small content of paramagnetic spins (~4%); this is too small to be attributed to either phase of Ba<sub>3</sub>SrMo<sub>2</sub>O<sub>9</sub> and is hence due to minor magnetic impurities. Between  $T_1$  and  $T_2$  the fractions of the two phases vary as described above so that the data can only be modelled below  $T_2$  [Fig.S5]. Further details of the fit are provided in the Supplementary Information [29].

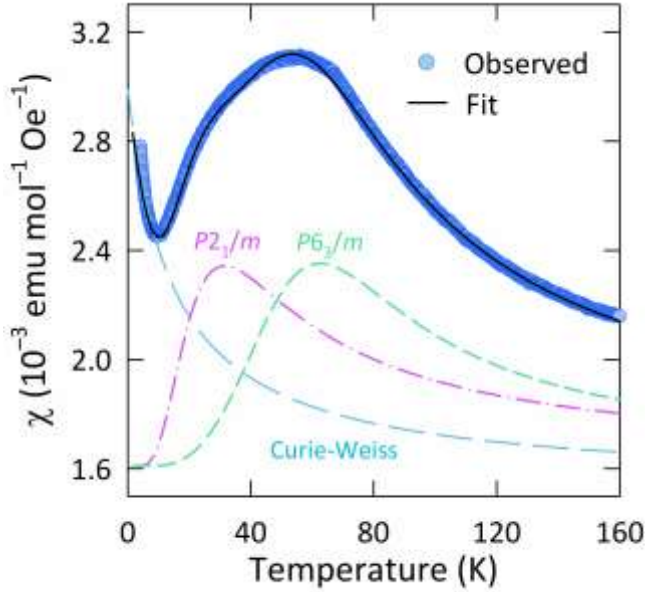


**Fig. 8.** ZFC DC magnetic susceptibility ( $\chi$ ) of  $\text{Ba}_3\text{SrMo}_2\text{O}_9$  under an applied field of  $H = 100$  Oe. Observed data points are given in blue, the fit to the interacting two-dimer model is given by the solid black line, and contributions from the two phases and the Curie-Weiss tail are given by the dashed lines;  $R^2 = 0.99893$ .

The intradimer exchange constants extracted from the fit in Fig. 8 are  $J_0/k_B(1) = 100.1(2)$  K and  $J_0/k_B(2) = 50(1)$  K for the  $P6_3/m$  and  $P2_1/m$  phases, respectively. This shows the  $P6_3/m$  phase contains spin-gapped  $\text{Mo}_2\text{O}_9$  dimers with stronger intradimer interactions compared to the  $P2_1/m$  phase so that exchange pathways are enhanced in the  $P6_3/m$  phase compared to the  $P2_1/m$  phase. The overall distortion of the  $\text{Mo}_2\text{O}_9$  dimers in the two phases are compared in Fig. S6, which demonstrates that there is greater distortion of the  $\text{MoO}_6$  octahedra in the  $P2_1/m$  phase. Distorting the dimers away from ideality disrupts the underlying Mo–O–Mo exchange pathways resulting in reduced intradimer interactions between the  $\text{Mo}^{5+}$  centers in the  $P2_1/m$   $\text{Mo}(1)$  dimers.

The absence of long-range magnetic order down to 1.6 K from both high intensity neutron diffraction and heat capacity demonstrates the  $\text{Mo}_2\text{O}_9$  spin dimers in both phases have singlet ground states. Spin dimers then form in  $\text{Ba}_3\text{SrMo}_2\text{O}_9$  in a similar fashion to other weakly

interacting quantum dimer magnets such as  $\text{Ba}_3\text{Mn}_2\text{O}_8$  [50] and  $\text{Sr}_3\text{Cr}_2\text{O}_8$  [51], where  $M-M$  distances are too great for direct  $M-M$  bonding to occur yet magnetic exchange interactions are sufficient to enable localized spins to condense and pair. Phase separation in  $\text{Ba}_3\text{SrMo}_2\text{O}_9$  is hence unrelated to competing magnetic orders at low temperatures.

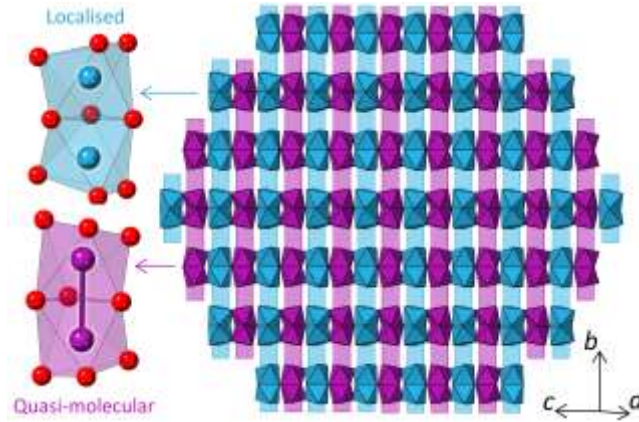


**Fig. 9.** Expanded view of the  $P2_1/m$  phase, showing how stripes of quasi-molecular  $\text{Mo}_2\text{O}_9$  clusters alternate with localized  $\text{Mo}_2\text{O}_9$  spin dimers along the monoclinic  $[001]$  direction.

$\text{Mo}_2\text{O}_9$  dimers are ordered in the  $P2_1/m$  phase such that stripes of quasi-molecular dimers alternate with localized AFM spin dimers along the monoclinic  $c$  axis (Fig. 9). Orbital hybridization and molecular clustering is hence confined to stripes of Mo–Mo bonded dimers, as opposed to the orbitally disordered and translation-invariant  $P6_3/m$  dimers. A very similar dimer configuration is encountered in charge-ordered  $\text{Ba}_3\text{NaRu}_2\text{O}_9$ , in which stripes of  $\text{Ru}^{5+}_2\text{O}_9$  and  $\text{Ru}^{6+}_2\text{O}_9$  dimers form due to the inherent geometric frustration associated with AFM dimers on a hexagonal crystal lattice [24]. This geometric frustration then underpins stripe formation in  $\text{Ba}_3\text{SrMo}_2\text{O}_9$  and further explains why no long-range magnetic order prevails in this system.

Electronic structure calculations have previously shown that there is a delicate balance between bonding and magnetic exchange in isostructural  $\text{Ba}_3\text{BiIr}_2\text{O}_9$  [48]. Below 74 K a 4% increase in

intradimer Ir–Ir distance breaks the Ir–Ir bond, resulting in electron localization and local moment formation. In comparison, the  $\sim 3.6\%$  reduction in half the  $P2_1/m$  Mo–Mo distances below  $T_{PS}$  in  $Ba_3SrMo_2O_9$  shows Mo–Mo bonding is favored over magnetic exchange below  $T_{PS}$ . No phase segregation was reported for  $Ba_3BiIr_2O_9$ , showing the underlying competition is insufficient to produce EPS. Competition between  $M$ – $M$  bonding and magnetic exchange appears to be enhanced for  $M = Mo$  compared to the  $M = Ru$  and Ir analogues. Furthermore, this competition in  $Ba_3SrMo_2O_9$  is remarkable as it establishes a new mechanism of EPS in electronic materials. This mechanism contrasts established electronic materials such as CMR manganites, where it is thought that disorder induced by chemical doping is essential for the observation of EPS [52, 53]. We observe no disorder between the Sr and Mo sites in  $Ba_3SrMo_2O_9$  to explain the extent of observed separation, nor do we find evidence of significant oxygen deficiency. As such,  $Ba_3SrMo_2O_9$  is an apparently unique electronic material where segregation is not induced via structural or chemical disorder but is instead intrinsic to the underlying electronic properties of the system.

## SUMMARY

Fundamentally,  $Ba_3SrMo_2O_9$  offers a stark contrast to prior EPS materials. A highly unusual mixture of ground states is encountered consisting of quasi-molecular  $Mo_2O_9$  dimers and  $Mo_2O_9$  spin dimers. Competition between Mo–Mo bonding and magnetic exchange drives EPS and appears to be independent of chemical disorder. Inelastic neutron scattering measurements are warranted to further explore this complex behavior. Chemical doping strategies also offer a promising route to attain a fully molecular or localized ground state. Such materials may find application in future orbitronic technologies and/or present new pathways to observe further exotic quantum phenomena such as spin-liquid properties. The observation of EPS in  $Ba_3SrMo_2O_9$  thus

demonstrates the potential of novel  $\text{Mo}^{5+}$  oxides to exhibit fascinating ground states and highlights a currently underexplored phase space in which to study complex electronic matter.

## ACKNOWLEDGEMENTS

We thank the Carnegie Trust for the Universities of Scotland for a PhD Scholarship for S.S. We acknowledge STFC-GB for provision of beamtime at the ILL. We also thank Dr. Mark Senn (University of Warwick) for useful discussions.

## REFERENCES

- [1] A. Moreo, S. Yunoki, and E. Dagotto, *Science* **283**, 2034 (1999).
- [2] M. Uehara, S. Mori, C. H. Chen, and S. W. Cheong, *Nature* **399**, 560 (1999).
- [3] T. Wu, S. B. Ogale, J. E. Garrison, B. Nagaraj, A. Biswas, Z. Chen, R. L. Greene, R. Ramesh, T. Venkatesan, and A. J. Millis, *Phys. Rev. Lett.* **86**, 5998 (2001).
- [4] E. Dagotto, *Nanoscale Phase Separation and Colossal Magnetoresistance* (Springer-Verlag, Berlin, 2003).
- [5] K. H. Ahn, T. Lookman, and A. R. Bishop, *Nature* **428**, 401 (2004).
- [6] E. Dagotto, *Science* **309**, 257 (2005).
- [7] J. P. Chapman, J. P. Attfield, L. M. Rodriguez-Martinez, L. Lezama, and T. Rojo, *Dalt. Trans.* 3026 (2004).
- [8] E. Dagotto, T. Hotta, and A. Moreo, *Phys. Rep.* **344**, 1 (2001).

- [9] E. Dagotto, *New J. Phys.* **7**, 67 (2005).
- [10] T. Dey, A. V. Mahajan, P. Khuntia, M. Baenitz, B. Koteswararao, and F. C. Chou, *Phys. Rev. B* **86**, 140405(R) (2012).
- [11] T. Dey, M. Majumder, J. C. Orain, A. Senyshyn, M. Prinz-Zwick, S. Bachus, Y. Tokiwa, F. Bert, P. Khuntia, N. Büttgen, A. A. Tsirlin, and P. Gegenwart, *Phys. Rev. B* **96**, 174411 (2017).
- [12] I. Terasaki, T. Igarashi, T. Nagai, K. Tanabe, H. Taniguchi, T. Matsushita, N. Wada, A. Takata, T. Kida, M. Hagiwara, K. Kobayashi, H. Sagayama, R. Kumai, H. Nakao, and Y. Murakami, *J. Phys. Soc. Jpn.* **86**, 033702 (2017).
- [13] W. J. Lee, S. H. Do, S. Yoon, S. Lee, Y. S. Choi, D. J. Jang, M. Brando, M. Lee, E. S. Choi, S. Ji, Z. H. Jang, B. J. Suh, and K. Y. Choi, *Phys. Rev. B* **96**, 014432 (2017).
- [14] A. Nag, S. Middey, S. Bhowal, S. K. Panda, R. Mathieu, J. C. Orain, F. Bert, P. Mendels, P. G. Freeman, M. Mansson, H. M. Ronnow, M. Telling, P. K. Biswas, D. Sheptyakov, S. D. Kaushik, V. Siruguri, C. Meneghini, D. D. Sarma, I. Dasgupta, and S. Ray, *Phys. Rev. Lett.* **116**, 097205 (2016).
- [15] S. V. Streltsov and D. I. Khomskii, *Phys. Rev. B* **89**, 161112(R) (2014).
- [16] D. I. Khomskii, K. I. Kugel, A. O. Sboychakov, and S. V. Streltsov, *J. Exp. Theor. Phys.* **122**, 484 (2016).
- [17] Y. Doi, Y. Hinatsu, Y. Shimojo, and Y. Ishii, *J. Solid State Chem.* **161**, 113 (2001).
- [18] Y. Doi, K. Matsuhira, and Y. Hinatsu, *J. Solid State Chem.* **165**, 317 (2002).

- [19] Y. Doi and Y. Hinatsu, *J. Mater. Chem.* **12**, 1792 (2002).
- [20] Y. Doi and Y. Hinatsu, *J. Phys. Condens. Matter.* **16**, 2849 (2004).
- [21] T. Sakamoto, Y. Doi, and Y. Hinatsu, *J. Solid State Chem.* **179**, 2595 (2006).
- [22] S. V. Streltsov and D. I. Khomskii, *Proc. Natl. Acad. Sci.* **113**, 10491 (2016).
- [23] M. Harland, A. I. Poteryaev, S. V. Streltsov, and A. I. Lichtenstein, *Phys. Rev. B* **99**, 045115 (2019).
- [24] S. A. J. Kimber, M. S. Senn, S. Fratini, H. Wu, A. H. Hill, P. Manuel, J. P. Attfield, D. N. Argyriou, and P. F. Henry, *Phys. Rev. Lett.* **108**, 217205 (2012).
- [25] D. Ziat, A. A. Aczel, R. Sinclair, Q. Chen, H. D. Zhou, T. J. Williams, M. B. Stone, A. Verrier, and J. A. Quilliam, *Phys. Rev. B* **95**, 184424 (2017).
- [26] Q. Chen, S. Fan, K. M. Taddei, M. B. Stone, A. I. Kolesnikov, J. Cheng, J. L. Musfeldt, H. Zhou, and A. A. Aczel, *J. Am. Chem. Soc.* **141**, 9928 (2019).
- [27] M. S. Senn, A. M. Arevalo-Lopez, T. Saito, Y. Shimakawa, and J. Paul Attfield, *J. Phys. Condens. Matter.* **25**, 496008 (2013).
- [28] C. A. López, M. E. Saleta, J. C. Pedregosa, R. D. Sánchez, D. G. Lamas, J. A. Alonso, and M. T. Fernández-Díaz, *J. Alloys Compd.* **661**, 411 (2016).
- [29] See Supplemental Material at [URL will be inserted by publisher], which includes Refs. [30–36], for additional refinement results and structural parameters for the  $P6_3/m$  phase of  $\text{Ba}_3\text{SrMo}_2\text{O}_9$ , magnetic susceptibility data and fits, and experimental methods.

- [30] J. Cumby and J. P. Attfield, *Nat. Commun.* **8**, 14235 (2017).
- [31] H. M. Rietveld, *Acta Crystallogr.* **22**, 151 (1967).
- [32] A. C. Larson and R. B. Von Dreele, Los Alamos National Laboratory Report, General Structure Analysis System (GSAS), Technical Report No. LAUR86-748 (2004).
- [33] B. H. Toby, *J. Appl. Cryst.* **34**, 210 (2001).
- [34] W. Miiller, M. Avdeev, Q. Zhou, A. J. Studer, B. J. Kennedy, G. J. Kearley, and C. D. Ling, *Phys. Rev. B* **84**, 220406(R) (2011).
- [35] I. W. Boyd, I. G. Dance, A. E. Landers, and A. G. Wedd, *Inorg. Chem.* **18**, 1875 (1979).
- [36] Y. Horibe, M. Shingu, K. Kurushima, H. Ishibashi, N. Ikeda, K. Kato, Y. Motome, N. Furukawa, S. Mori, and T. Katsufuji, *Phys. Rev. Lett.* **96**, 086406 (2006).
- [37] R. D. Shannon, *Acta Crystallogr. Sect. A* **32**, 751 (1976).
- [38] P. W. Stephens, *J. Appl. Crystallogr.* **32**, 281 (1999).
- [39] S. Nakatsuji, K. Kuga, K. Kimura, R. Satake, N. Katayama, E. Nishibori, H. Sawa, R. Ishii, M. Hagiwara, F. Bridges, T. U. Ito, W. Higemoto, Y. Karaki, M. Halim, A. A. Nugroho, J. A. Rodriguez-Rivera, M. A. Green, and C. Broholm, *Science* **336**, 559 (2012).
- [40] C. Garg, D. Roy, M. Lonsky, P. Manuel, A. Cervellino, J. Müller, M. Kabir, and S. Nair, *Phys. Rev. B* **103**, 014437 (2021).
- [41] B. Rowda, M. Avdeev, P. L. Lee, P. F. Henry, and C. D. Ling, *Acta Crystallogr. Sect. B* **64**, 154 (2008).

- [42] C. D. Ling, B. Rowda, M. Avdeev, and R. Pullar, *J. Solid State Chem.* **182**, 479 (2009).
- [43] M. T. Dunstan, A. F. Pavan, V. V. Kharton, M. Avdeev, J. A. Kimpton, V. A. Kolotygin, E. V. Tsipis, and C. D. Ling, *Solid State Ionics* **235**, 1 (2013).
- [44] K. E. Stitzer, M. D. Smith, W. R. Gemmill, and H. C. Zur Loye, *J. Am. Chem. Soc.* **124**, 13877 (2002).
- [45] J. P. Attfield, *APL Mater.* **3**, 041510 (2015).
- [46] K. H. Hong, A. M. Arevalo-Lopez, J. Cumby, C. Ritter, and J. P. Attfield, *Nat. Commun.* **9**, 2975 (2018).
- [47] B. Bleaney and K. D. Bowers, *Proc. R. Soc. London. Ser. A* **214**, 451 (1952).
- [48] W. Miiller, M. Avdeev, Q. Zhou, B. J. Kennedy, N. Sharma, R. Kutteh, G. J. Kearley, S. Schmid, K. S. Knight, P. E. R. Blanchard, and C. D. Ling, *J. Am. Chem. Soc.* **134**, 3265 (2012).
- [49] A. J. Browne, C. Lithgow, S. A. J. Kimber, and J. P. Attfield, *Inorg. Chem.* **57**, 2815 (2018).
- [50] M. Uchida, H. Tanaka, M. I. Bartashevich, and T. Goto, *J. Phys. Soc. Jpn.* **70**, 1790 (2001).
- [51] Y. Singh and D. C. Johnston, *Phys. Rev. B* **76**, 012407 (2007).
- [52] Y. Zhu, K. Du, J. Niu, L. Lin, W. Wei, H. Liu, H. Lin, K. Zhang, T. Yang, Y. Kou, J. Shao, X. Gao, X. Xu, X. Wu, S. Dong, L. Yin, and J. Shen, *Nat. Commun.* **7**, 11260 (2016).
- [53] T. Miao, L. Deng, W. Yang, J. Ni, C. Zheng, J. Etheridge, S. Wang, H. Liu, H. Lin, Y. Yu, Q. Shi, P. Cai, Y. Zhu, T. Yang, X. Zhang, X. Gao, C. Xi, M. Tian, X. Wu, H. Xiang, E. Dagotto, L. Yin, and J. Shen, *Proc. Natl. Acad. Sci.* **117**, 7090 (2020).